Study of the Influence of the Lack of Contact in Plate and Fin and Tube Heat Exchanger on Heat Transfer Efficiency under Periodic Flow Conditions

Marcin Łęcki *, Dariusz Andrzejewski, Artur N. Gutkowski [ID] **and Grzegorz Górecki**

Faculty of Mechanical Engineering, Institute of Turbomachinery, Lodz University of Technology, 219/223 Wolczanska Street, 90-924 Lodz, Poland; dariusz.andrzejewski@p.lodz.pl (D.A.); artur.gutkowski@p.lodz.pl (A.N.G.); grzegorz.gorecki@p.lodz.pl (G.G.)
* Correspondence: marcin.lecki@p.lodz.pl; Tel.: +48-42631-23-20

Abstract: Plate fin-tube heat exchangers are widely used in air conditioning and refrigeration systems and other industry fields. Various errors made in the manufacturing process can result in the formation of an air gap between the tube and fin. Several numerical simulations were carried out for a symmetric section of plate fin-tube heat exchanger to study the influence of air gap on heat transfer under periodic flow conditions. Different locations and sizes of an air gap spanning 1/2 circumference of the tube were considered for the range of airflow velocities. Velocity and temperature fields for cases with air gap were compared with ideal thermal contact cases. Blocking of heat flow by the gap leads to the reduction of heat transfer rate. Fin discontinuity in the front of the tube causes the smallest reduction of the heat transfer rate in comparison to the ideal tube-fin contact, especially for thin slits. The rear gap position is the worst in the smallest gap range. Therefore, reversing the flow direction can lead to up to a 15% heat transfer increase, if mainly the rear gaps are present. The introduction of a thin slit in the front of the tube leads to convective heat transfer enhancement, which should be further investigated.

Keywords: heat exchanger; plate-fin tube; tube-fin contact; CFD

1. Introduction

Plate-fin and tube heat exchangers are most widely used as evaporators and condensers in refrigeration systems (commercial refrigeration) and in other applications where heat transfer between liquid or evaporating/condensing fluid and gaseous working fluid is required. Proven technology, reliability, and relatively low cost of manufacture make plate-fin and tube heat exchangers very popular, not only as components of refrigeration units but also as gas coolers/heaters, recuperative heaters, dryers or heat pipe, thermosyphon radiators [1–3]. Nowadays, when detailed numerical simulations of fluid flow with heat transfer are within reach, many of the researchers carry out Computational Fluid Dynamics (CFD) studies to optimize the geometry of plate-fin and tube heat exchangers [4,5]. The majority of these works assume an ideal tube fin contact that in practice has to be created during the manufacturing process. The contact is usually achieved by a tube expansion (plastic deformation of the tube by moving the expansion die or by applying pressure at its inner surface). These mechanical methods of expansion cause additional thermal resistance at the tube–fin interface, due to the gaps between the contact surfaces of the fin collars and tubes [4]. Formation of the gap can be also a result of the nonideal joint formation process or assembly requirements. For the egg-crate-type heat exchangers, which are used as evaporators in domestic refrigerators, slits between the tubes are introduced to allow one to pull the whole tube coil through the plate-fin packet [6]. In this case, the lack of contact is always present at approximately 1/2 perimeter of the tube, and it is a feature essential for the assembly of the heat exchanger.

The gaps can be also created because of the wear of the heat exchanger, e.g., as the result of corrosion by exposure to difficult weather conditions or by strong chemical interactions. In Figure 1, one can see a picture (courtesy of Blygold company [7]) of a corroded heat exchanger surface with gaps on the circumference of the tube. In this case, fin discontinuities are just one of the factors affecting heat transfer; there are also white corrosion products around the tubes that impede heat transfer (AlOH thermal conductivity is smaller than for Al).
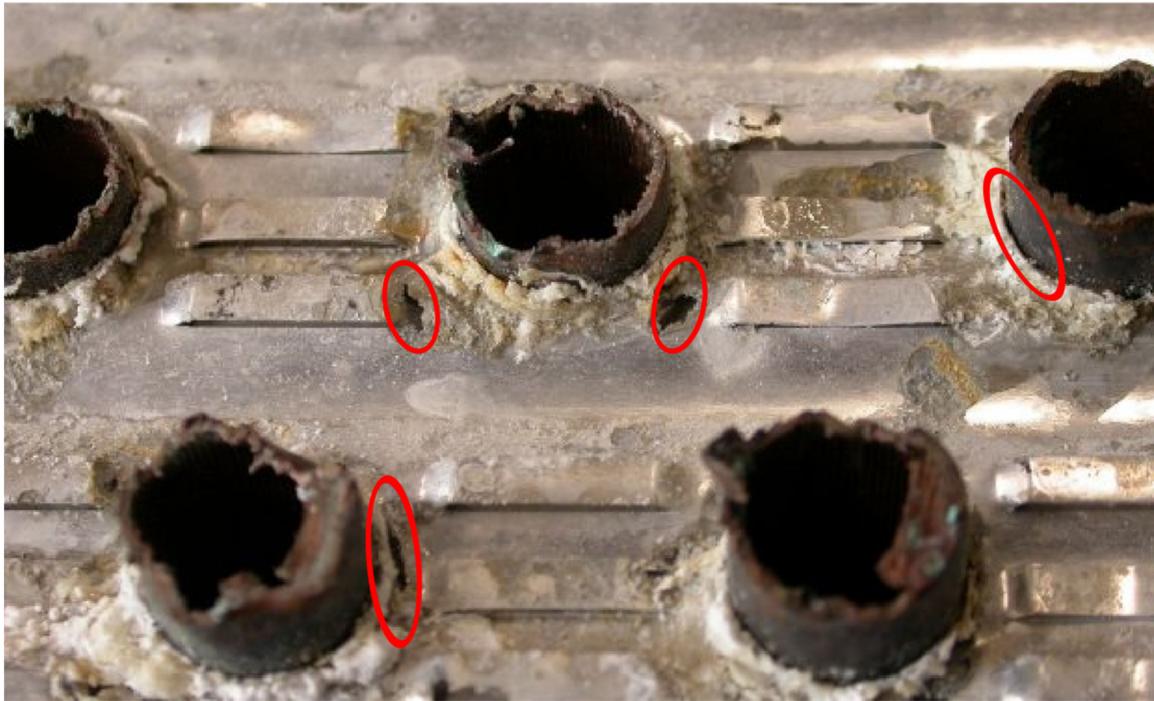

Figure 1. Gaps in the fin on the circumference of the tube created by a corrosion process, marked areas in the Figure (photo provided by courtesy of Blygold company [7]).

The quality of the joint can be improved by brazing the tube to the fin (the soldering process and its impact on heat transfer are discussed in detail in [8–10]). Because of the additional amount of energy needed for the soldering process and some technical difficulties (ensuring high purity of soldered surfaces), mechanical methods of expansion are most frequently chosen. Non-ideal tube fin connection can cause significant thermal contact resistance which deteriorates heat transfer. Therefore, some of the researchers have undertaken studies taking into account the realistic fin-tube thermal contact and its impact on the thermal efficiency of heat exchangers. Aside from the experimental research aimed at estimating the thermal contact resistance [11,12], its value is also obtained through semiempirical methods, partly based on numerical analysis. Taler and Oclon [13] and Taler and Cebula [14] changed iteratively the value of contact resistance in their CFD model in such a way that the thermal and flow quantities obtained from the numerical solution agreed with the measured ones. Less attention has been paid to cases where there is a lack of contact with the plate-fin along a part of the tube perimeter (no contact between the fin collar and tube). Recently, the topic was addressed by Singh et al. [15] who proposed a CFD model of a finned heat exchanger with a variable contact surface area between the tube and the fin. They considered several cases of gaps of different sizes. They found that the presence of gaps influenced heat transfer and flow (pressure drop) in a significant way. In contrast to [15], where several triangular gaps are distributed evenly along the joint circumference, our work presents a CFD analysis of plate-fin and tube heat exchanger, where there is a lack of contact between the tube and the fin at the half of the tube's circumference. The present study aims to numerically investigate the effect of the

lack of contact on the energy efficiency of the heat exchanger for variable parameters, such as different air velocities and various positions of the gap relative to the flow direction. The CFD model is developed with the assumption of periodic flow boundary conditions. The novelty of the present work lies mostly in the consideration of the different locations and sizes of the gaps between the tube and fin relative to the flow direction. Because of the nonuniform heat transfer coefficients on the fin and tube surfaces, the expected degree of heat transfer deterioration is a function of the position of the cavity. Only in [15] was a similar CFD analysis done, but evenly distributed triangular voids excluded the possibility of dependency on the flow direction; additionally, the authors of [15] considered a slightly different geometry of the plate-fin tube heat exchanger than the typical one (with slitted fins). The present work assumes more realistic positions of gaps resulting from wear (corrosion) or erroneous tube expansion in the classic type of plate-fin tube heat exchanger. It contributes to the current area of research by expanding knowledge about the magnitude of heat transfer deterioration (fin efficiency) caused by the lack of contact between fin and tube depending on flow conditions. It can help to understand and predict the thermal effects of wear and manufacture errors on the functioning of compact heat exchangers.

2. Numerical Model of a Heat Exchanger

The heat exchanger under consideration works as a condenser in a refrigeration system. It is a plate-fin and tube heat exchanger, in which tubes are arranged in-line. It was recognized that the location of the gap relative to the flow direction is an important parameter because of the variation in the local heat transfer coefficients on the surface of the fin and the locally variable velocity field [16]. The gap location along tube-fin joint circumference should therefore have a significant impact on heat exchange and flow patterns. Figure 2 shows the analyzed configurations.
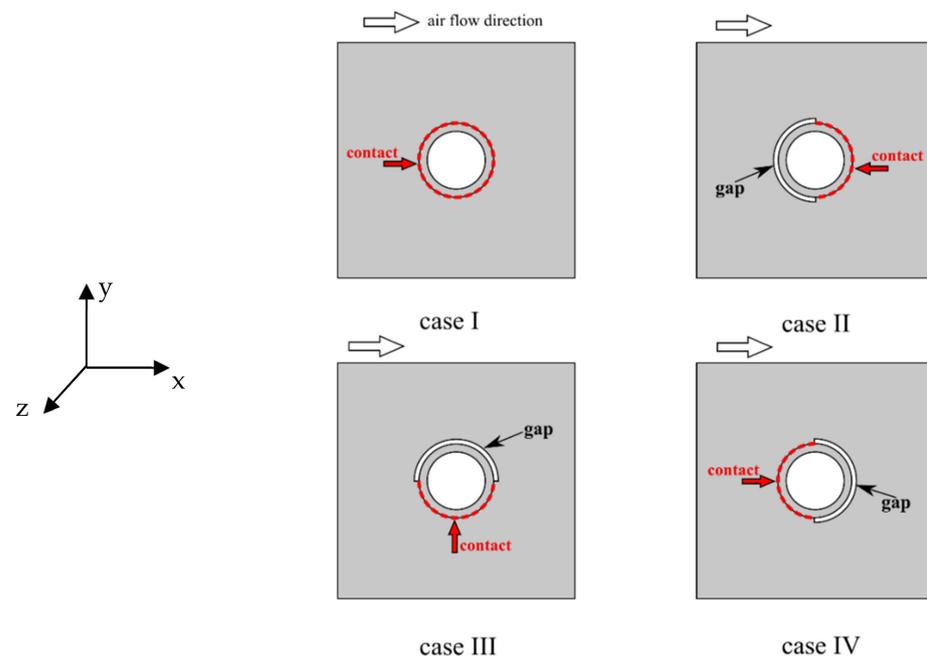

Figure 2. Different positions of the gap with respect to airflow: Case I—without gap; Case II—the gap in the front of the tube; Case III—the gap in the top position; Case IV—gap in the back of the tube.

Case I (without a gap—thickness of discontinuity $\delta = 0$ mm) is treated as a reference. The slit position is nondimensionalized as $\theta/180°$, where θ is an angular position. In the second case, the gap spans the front side of the circumference ($\theta = 0°$). In Case III, it is placed on the upper half perimeter ($\theta = 90°$), in the last IV variant—in the back of the tube ($\theta = 180°$). The angles indicate the centers of the gaps, taking into account the slit circumference span the corresponding angle ranges are front gap ($90° \leq \theta \leq 270°$), top gap ($0° \leq \theta \leq 180°$),

and back gap ($-90° \leq \theta \leq 90°$). Four gap thicknesses were taken into account: 0.25, 0.5, 1.0, and 2 mm, corresponding to the following dimensionless values (relative to tube diameter): 0.03125, 0.0625, 0.125, and 0.25. Numerical simulations were carried out for airflow through the heat exchanger equal to 1, 2, 3, 4, and 5 m/s average velocities at the flow area directly upstream of the entrance to the device under consideration.

2.1. Geometry of the Computational Domain

The computational domain is a repeatable slice of the heat exchanger geometry, which is shown in Figure 3. The length and width of the domain are equal to the distance between axes of the tubes L_f. The thickness of the fin in the computational domain is half of the actual fin thickness δ_f, as the temperature field is symmetric at the opposite half of the fin (see the symmetry plane in Figure 3). Tube length in the domain equals $\frac{1}{2}$ of the distance between fins. Taking the half of inter-fin spacing is a consequence of the flow symmetry assumption. The actual domain boundary is marked in Figure 3 by a dashed line and spans up to the symmetry plane. The specific dimensions of the domain are given in Table 1.
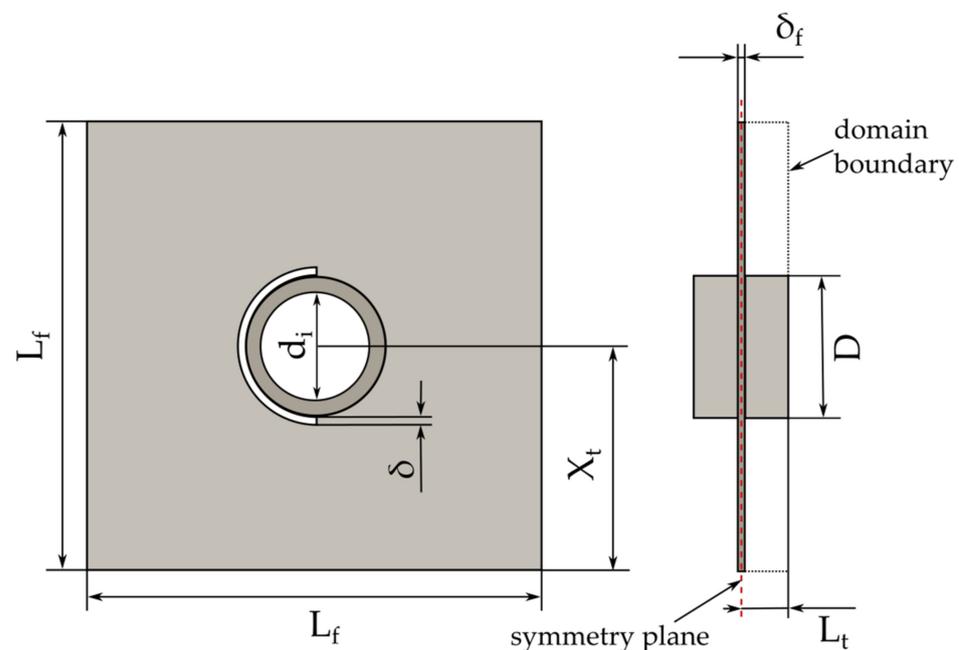
Figure 3. The geometry the simulated slice of the heat exchanger.

Table 1. The dimensions of the domain for the analyzed cases.

Description	Symbol	Value [mm]
Length and width of the fin	Lf	25
Tube length	Lt	2.5
Outside diameter of the tube	D	8
Internal diameter of the tube	di	6.2
Fin thickness	δ_f	0.05
Gap thickness	δ	0.25–2.0
Tube spacing	X_t	12.5

2.2. Boundary Conditions and Governing Equations

The shear stress transport (SST) turbulence model was chosen to solve Reynolds (time) averaged Navier-Stokes equations (RANS). SST combines the best features of *k-ε*

and k-ω models. In the near-wall region, approximately up to half of the boundary layer k-ω formulation is used, which does not require any damping functions, while for the outer zone of the boundary layer k-ε is the governing turbulence model—it eliminates the problem of k-ω sensitivity to values of ω in the freestream (outside the boundary layer). The other advantage of SST is the accurate prediction of the boundary layer separation by application of the turbulence production limiter in stagnation regions [17]. The SST model is also characterized by very good accuracy of the numerical solutions for wall-bounded, complicated geometry flows, obtained with relatively low computational power. Recently, Lindqvist et al. have performed an extensive analysis of RANS turbulence models in the application to numerical simulation of airflow and heat transfer in plate-fin and tube heat exchangers [18]. The k-ω SST was chosen as optimal and used for further validation against experimental data. It was utilized in many works where CFD analysis of the heat transfer for finned and enhanced surfaces was carried out [4,13,19–21].

The following simplifying assumptions were made in the present work:

- Steady-state fluid flow and heat transfer;
- Fluid flow and heat transfer are periodic (fully-developed), meaning that pattern of flow/thermal solution has a periodically repeating nature (this condition is generally fulfilled for tube rows greater than the fourth row);
- Thermophysical properties of air are temperature-dependent (ideal gas);
- Natural convection was not considered as the highest Richardson number calculated for simulation conditions is $Ri = (g{\cdot}\beta{\cdot}\Delta T{\cdot}L)/u^2 = 0.025$ (for $Ri < 0.1$ mechanism of natural convection can be typically considered negligible).

Numerical calculations were carried out using the commercial ANSYS CFX code capable of solving the Navier-Stokes equations [22]:

$$\frac{\partial u_i}{\partial x_i} = 0, \tag{1}$$

$$\rho \frac{\partial}{\partial x_j}\left(u_i u_j\right) = -\frac{\partial p}{\partial x_i} + \frac{\partial}{\partial x_j}\left(\tau_{ij} - \rho\overline{u_i u_j}\right) \tag{2}$$

where τ is a stress tensor in the fluid, and $\rho\overline{u_i u_j}$ are Reynolds stresses (turbulent), which depend on average velocity gradients (Boussinesq hypothesis):

$$-\rho\overline{u_i u_j} = \mu_t\left(\frac{\partial u_i}{\partial x_j} + \frac{\partial u_j}{\partial x_i}\right) - \frac{2}{3}\left(\rho k + \mu_t \frac{\partial u_k}{\partial x_k}\right)\delta_{ij} \tag{3}$$

where k—turbulence kinetic energy and μ_t—turbulent viscosity.

The SST turbulence model allows for obtaining turbulent viscosity by using two transport equations of kinetic turbulence energy k and specific dissipation rate ω. Due to the extensive definition of the model, it will not be presented here; its formulation can be found in [17]. The turbulent viscosity is calculated using the equation:

$$\mu_t = \rho \frac{k}{\omega} \tag{4}$$

The energy equation for fluid is given by:

$$\frac{\partial}{\partial x_i}[u_i(\rho{\cdot}e + p)] = \frac{\partial}{\partial x_j}\left[\left(\lambda + \frac{c_p \mu_t}{Pr_t}\right)\frac{\partial T}{\partial x_j}\right] \tag{5}$$

where e—total fluid energy, T—temperature, λ—thermal conductivity, c_p—specific heat at constant pressure, and Pr_t—turbulent Prandtl number for energy (assumed value: 0.9). In the solid body (fin and tube domain), the heat is exchanged by means of steady conduction:

$$\frac{\partial}{\partial x_j}\left(\lambda\frac{\partial T}{\partial x_j}\right) = 0 \tag{6}$$

The computational domain is divided into three parts: air (fluid), fin, and tube (solids). It was assumed that the thermal conductivity of the solid (aluminum) is constant in the tested temperature range, which is λ = 202.4 W/m/K. A periodic flow was solved with the following boundary conditions and parameters:

- Average air temperature at the inlet: T_{ave} = 22 °C,
- u = 0 m/s on the fin and tube surfaces (no-slip condition),
- Uniform temperature at the inner surface of the tube wall: T_w = 40 °C—which corresponds to the condensation conditions of the working fluid flowing inside the tube.

On the other surfaces of the computational domain, a symmetry boundary condition was assigned, which can be expressed mathematically as:

$$-\overline{n}\cdot\dot{q} = 0, \; u\cdot\overline{n} = 0, \; \nabla k\cdot\overline{n} = 0, \; \nabla\omega\cdot\overline{n} = 0 \tag{7}$$

where $\overline{n}$ is a normal vector to the surface on which the boundary condition was set. Additionally, on the solid–fluid contact surfaces, a coupled boundary condition was present, ensuring the energy balance is satisfied between domains.

The periodic condition of the velocity in the x-direction can be written as:

$$u_1(\overline{r}) = u_1(\overline{r} + \overline{L}) = u_1(\overline{r} + 2\overline{L}) = \ldots \tag{8}$$

where $\overline{r}$—position vector and $\overline{L}$—the periodic length vector (equations in the rest of the Cartesian directions are analogous).

For viscous flows, the pressure field is considered periodic if the following condition is met:

$$\Delta p = p(\overline{r}) - p(\overline{r} + \overline{L}) = p(\overline{r} + \overline{L}) - p(\overline{r} + \overline{2L}) = \ldots \tag{9}$$

The pressure gradient is divided into two parts: a periodic gradient and a linear gradient:

$$\nabla p(\overline{r}) = \beta\frac{\overline{L}}{|\overline{L}|} + \nabla\widetilde{p}(\overline{r}) \tag{10}$$

where $\widetilde{p}(\overline{r})$ is so-called periodic pressure and $\beta\frac{\overline{L}}{|\overline{L}|}$—linearly variable pressure component. Periodic pressure is the remainder after subtracting the linear pressure. On the other hand, the linearly variable component results in a force acting on the fluid in the momentum equations. During the solution process, the value of the coefficient β is iteratively changed until the desired convergence between the set and the calculated mass flow is obtained.

The temperature field is analogously divided into two components for periodic simulation:

$$T(\overline{r}) = \sigma|\overline{r}| + \widetilde{T}(\overline{r}) \tag{11}$$

where:

$$\sigma = \frac{\dot{Q}}{\dot{m}\cdot c_p\cdot L} \tag{12}$$

and $\dot{Q}$—net heat transfer rate in a periodic domain.

At the inlet and outlet, the periodic boundary condition has the form:

$$T(\overline{r}) = \widetilde{T}(\overline{r} + \overline{L}), \; p(\overline{r}) = p(\overline{r} + \overline{L}), \; u_1(\overline{r}) = u_1(\overline{r} + \overline{L}) \tag{13}$$

The above-mentioned conditions for the periodicity of the airflow are practically implemented in the Ansys-CFX CFD software. The boundaries named in Figure 4 as periodic inlet and periodic outlet are coupled as two flow interfaces; the target mass flow can be specified, which is obtained by iteratively changing the pressure gradient β. Negative heat flux has to be fixed at the periodic outlet boundary to balance the heat transfer rate gained by air flowing through the domain, as the outflowing fluid is "returned" to the inlet (Figure 4). If a heat sink is not introduced, the air temperature rises infinitely during the solution process of the numerical simulation, causing the solver to crash after reaching some maximum temperature level. In the case of numerical simulations carried out within this research, the domain was properly thermally balanced to keep the inlet temperature at an approximately constant level of 22 °C. The symmetry boundary condition is applied at domain boundaries that were not marked in Figure 4 (for both solid and fluid surfaces).

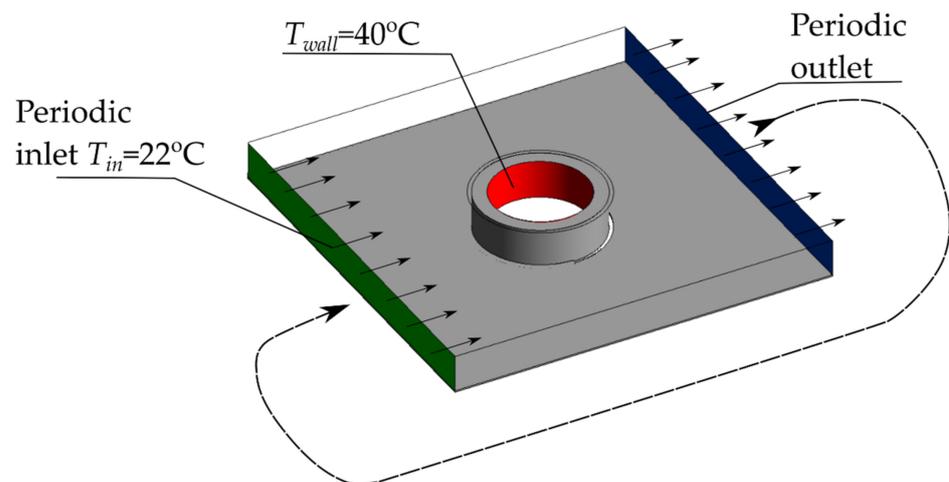**Figure 4.** Boundary conditions for the computational domain.

2.3. Computational Grid

Numerical simulations of the fluid flow with coupled heat exchange process were carried out using ANSYS CFX CFD software. The computational grid for the case I is shown in Figure 5. It was created for the repetitive slice of heat exchanger with the use of ANSYS-Meshing application.
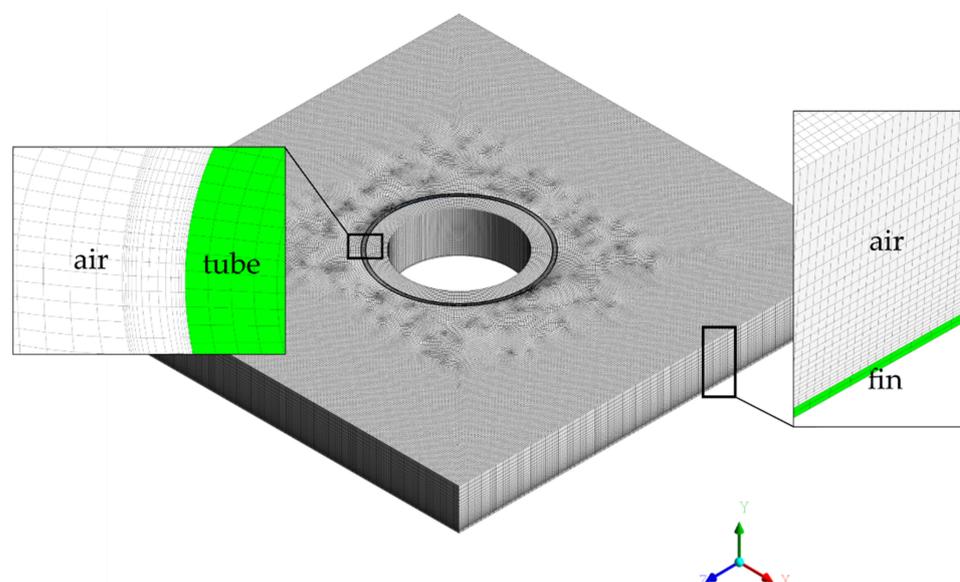

Figure 5. View of the computational mesh.

The grid independence study was performed using a methodology similar to used in works [23,24]. The five grids were tested, namely, coarse, average, fine, very fine, and the finest corresponding to mesh sizes: 0.2×10^6, 1.8×10^6, 2.14×10^6, 2.48×10^6, and 2.80×10^6 nodes. For all of the five meshes, the prism layer elements number at the wall was gradually increased, starting from 10 for the coarse grid by 25, 30, 35, up to 40 for the finest one. The Y^+ parameter and percent change of mean heat transfer coefficient $h_\%$ were presented in Figure 6. The $h_\%$ is the relative difference between the obtained average heat transfer coefficient for the ith mesh refinement level and $i - 1$ refinement (the one-step coarser mesh). The change does not exceed 0.5%; therefore, the average mesh (1.8×10^6 nodes) was chosen as optimal because it also satisfies the maximum $Y^+ < 1$ condition (maximum $Y^+ = 0.44$, average $Y^+ = 0.24$).
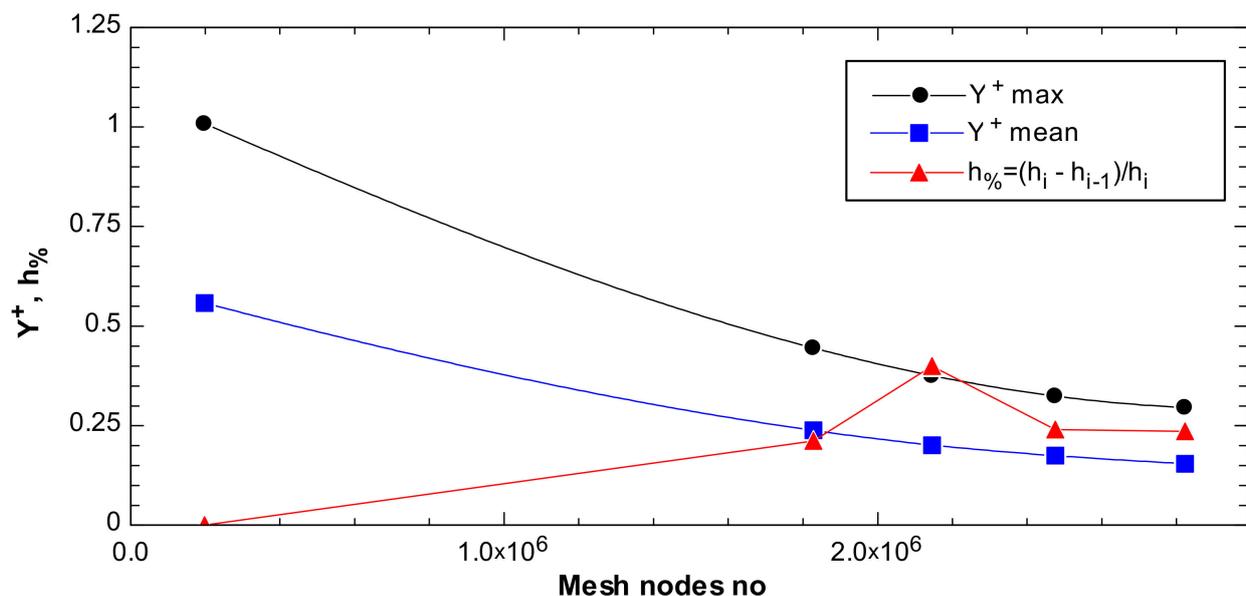

Figure 6. Dependence of an average and maximum Y^+ in the computational domain, and percent change of mean heat transfer coefficient $h_\%$ versus the number of mesh nodes.

2.4. Validation of the Numerical Model

The computational model was validated against data published in the work of Saboya and Sparrow [16] as their paper is widely acknowledged as the standard for validation of the studies of heat transfer from finned surfaces. They used the naphthalene sublimation technique [25] to obtain local mass transfer coefficients (Sherwood numbers *Sh*) on the fin surface of the one-row plate-fin tube heat exchanger. The Sherwood number distribution can be converted to heat transfer coefficients by utilization of the heat-mass transfer analogy:

$$h_{mass} = Sh \cdot \left(\frac{Pr}{Sc}\right)^n \cdot \left(\frac{\lambda}{d_h}\right) \tag{14}$$

where *Sc*—Schmidt number, d_h—hydraulic diameter according to Kays and London [26], and *n*—heat-mass transfer analogy exponent. Rosman et al. [27] have chosen the value of the $n = 0.4$ based on his experiment and measurements available in the literature. However, the latest careful measurements have reaffirmed that the most suitable value of the exponent for both laminar and turbulent boundary layers is approximately $n = 0.33$ [23]. Prandtl number and thermal conductivity are assumed as for pure air ($Pr = 0.7$, $\lambda = 0.026$ W/m/K)— the concentration of naphthalene is too low to significantly influence the thermophysical properties of the fluid. Saboya and Sparrow [16] assumed $Sc = 2.5$, yet it is an outdated value, and for room temperature the $Sc = 2.28$ is now recommended [25]. Local Sherwood numbers [16] were converted to heat transfer coefficients according to (14) and prepared to

validate the CFD simulation. On the left side of Figure 7, the distribution of heat transfer coefficients on the fin surface is shown obtained from [16] for *Re* = 214. The distribution of local *h* is only known along the horizontal black lines where the mass transfer coefficients are measured—a 2D contour map is a result of an inverse distance interpolation made in Tecplot 360 EX software [28]. On the right side, there are results from numerical simulation for analogous flow and thermal conditions as in the experimental work. This setup allows a direct comparison between two contour maps. As can be seen, the ranges of heat transfer coefficient values are nearly the same. Near the front edge of the fin, the convective heat transfer seems to be more intensive in the case of the numerical results, but the lower *h* are a consequence of the interpolation of the Saboya and Sparrow's [16] data from the location significantly upstream of the edge of the fin.
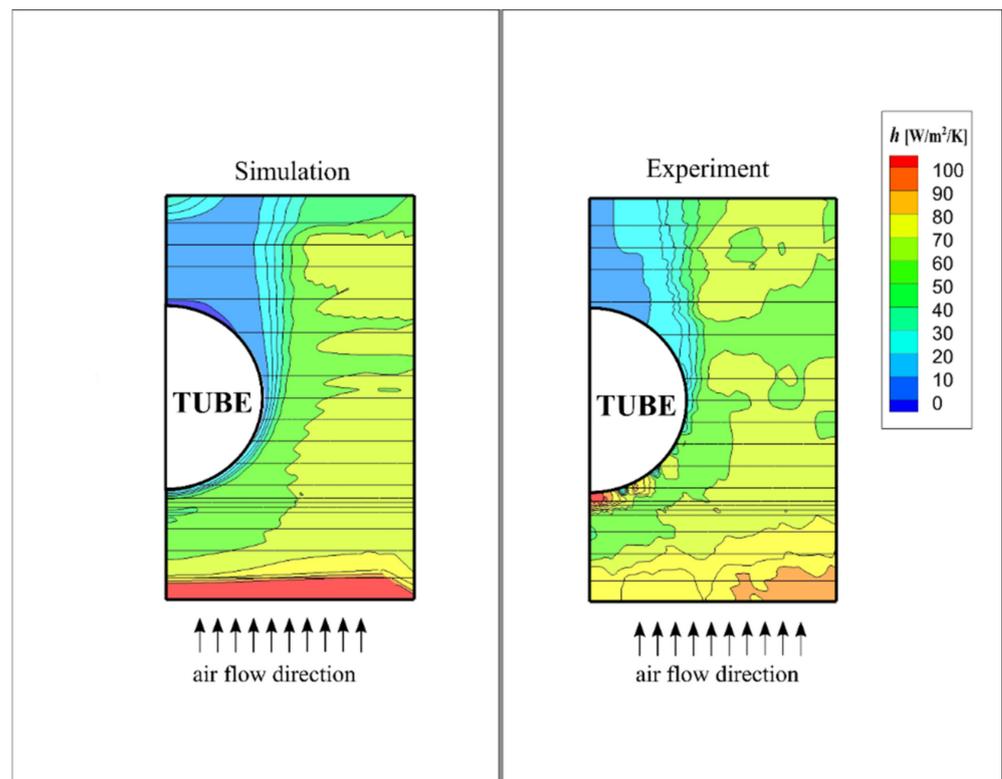

Figure 7. Comparison of local *h* on the surface of the fin between numerical simulation and experiment [16] for *Re* = 214.

The accordance of the simulation's local *h* with the experiment is shown in Figure 8. Four lines were chosen, where the measurements were taken exactly—at the front (line 1), back (line 4), and middle segments (lines 2, 3) of the fin. Most of the experimental data is in very good agreement with the CFD solution (maximally ±20% and better). The greatest discrepancies are noted in the near tube region, but they can be caused by the fact that in the experiment [16] the tube surface was adiabatic. The uncertainty of the experimental *h* was also plotted in the form of error bars. It was based on the estimation of the uncertainty of Sherwood number measurements done in [29] (uncertainty within 7.3%).
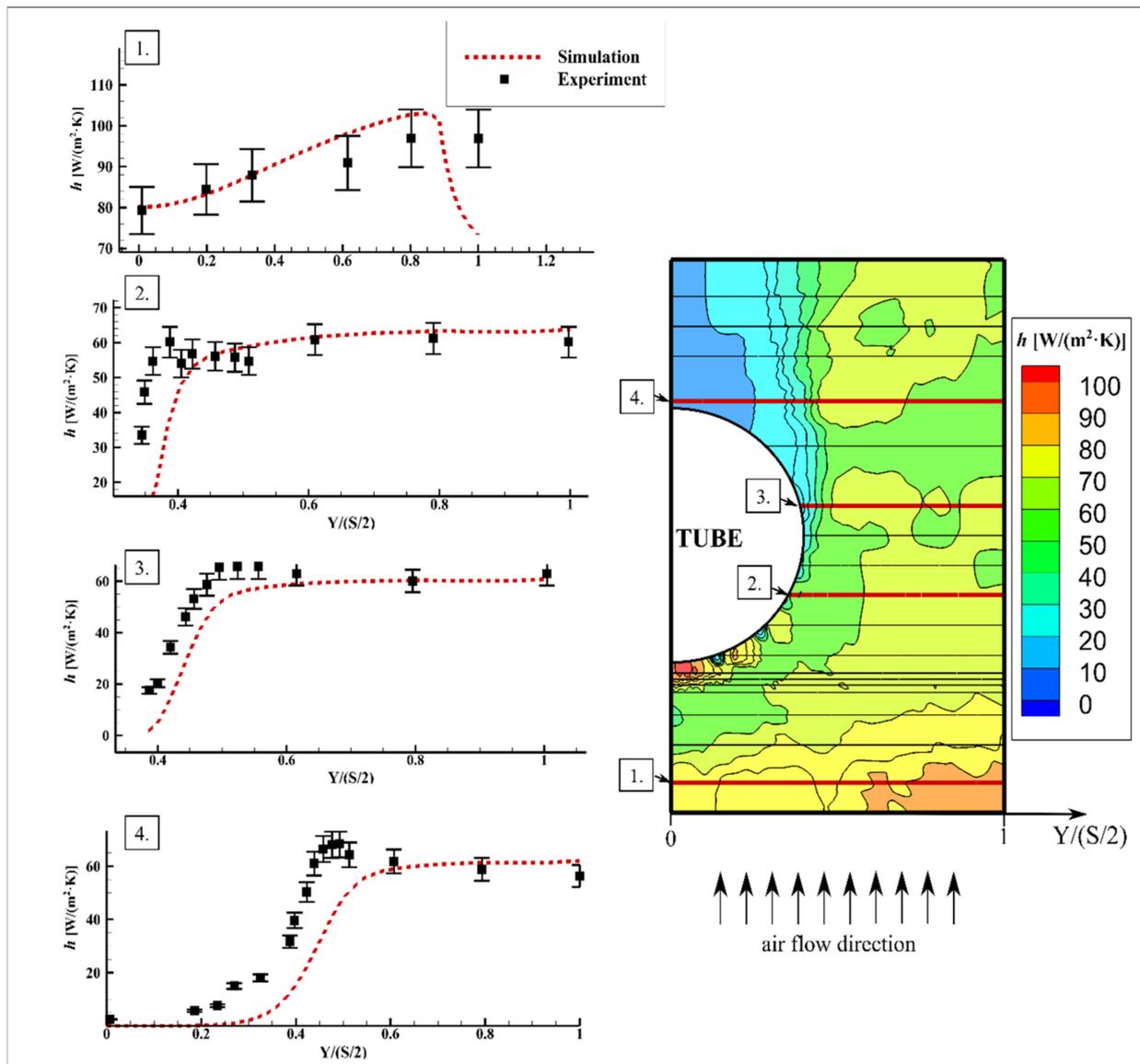
Figure 8. Local heat transfer coefficients from experiment versus CFD simulation at four lines transverse to the airflow at the front (line 1), back (line 4), and middle segments (lines 2, 3) of the fin for *Re* = 214.

The validation presented above was made to test the ability of the model to predict local coupled heat and fluid flow phenomena. Because the experimental flow arrangement (one-row tube-fin) is not adequate to the simulation settings (periodical flow—more than four-row inline tube-fin geometry), additional validation was performed. Mean heat transfer obtained from the simulation was compared against VDI correlation [30], which is true for three rows inline heat exchangers:

$$Nu_D = 0.20 Re_D^{0.6} \left(\frac{A}{A_{t0}} \right)^{-0.15} Pr^{1/3} \tag{15}$$

A comparison between simulation heat transfer coefficients and VDI correlation is presented in Figure 9. The two data sets' values are very close. The relative difference varies from 4.9% for the lowest *Re* to 1.8% for the biggest airflow.
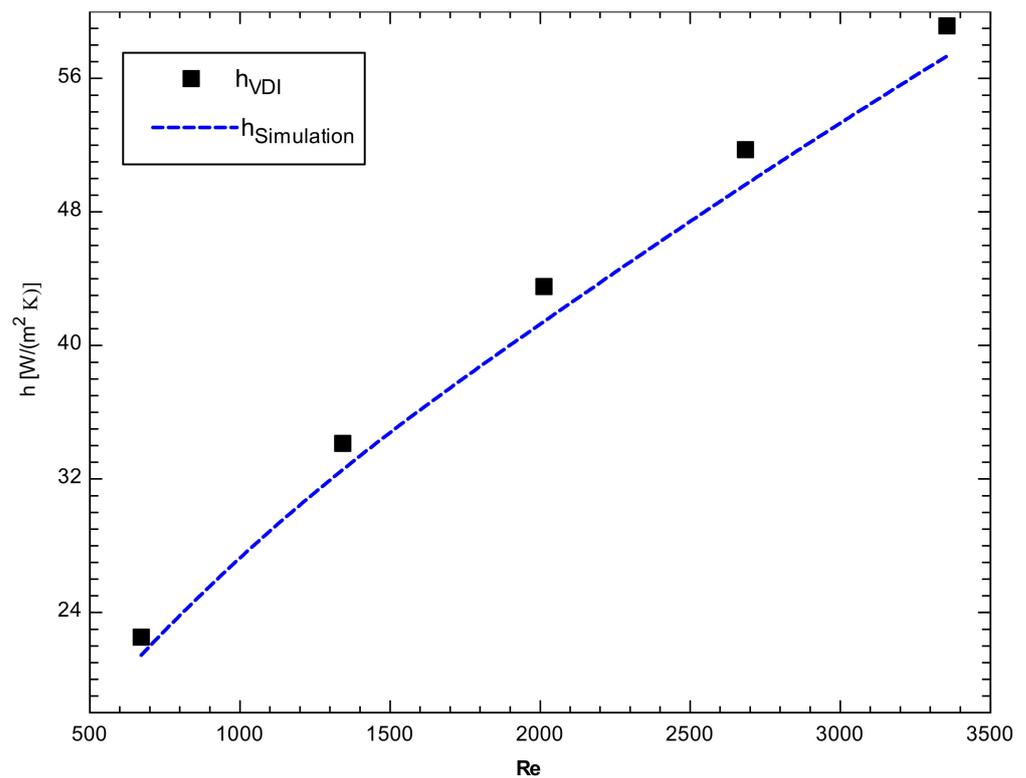
Figure 9. Comparison between heat transfer coefficients obtained from numerical simulation to the ones calculated with VDI correlation valid for three-row inline heat exchangers.

3. Results and Discussion

The results of the numerical simulations were put together in a form of a series of graphs, allowing for the evaluation of the thermal efficiency of the cases with the presence of the gap to perfect fin-tube contact example. In Figure 10, the ratios of heat transfer rates (discontinuity to no-slit heat transfer rate) are presented in the function of the dimensionless gap thickness (gap thickness to diameter). For each Reynolds number, a curve approximating the numerical data is presented. For the gap in the back and front, the minimal ratio of heat transfer rate is approx. 0.75 for the considered airflow span, whereas the side gap attains a slightly lower minimum of 0.72. For the front and side gap localization, there is a bigger spacing between the curves (stronger influence of the airflow velocity) than for the rear position. This effect is the strongest for smaller gaps. For $\delta/D > 0.1$, there is no significant difference between curves spacing for all examined cases. The shapes of the curves are similar for all the arrangements, although for the fin discontinuity in the rear of the tube the heat transfer ratio drop from unity ($\delta/D = 0$) is much steeper than for the other locations. Heat transfer rate ratios are significantly lower for back orientation, especially for small gap thickness and small Re. Usually the higher the Reynolds number the lower value of $\dot{Q}/\dot{Q}_0$, although there is an exception for the lowest considered Reynolds number curve for nearly all gaps, excluding the biggest fin discontinuity.
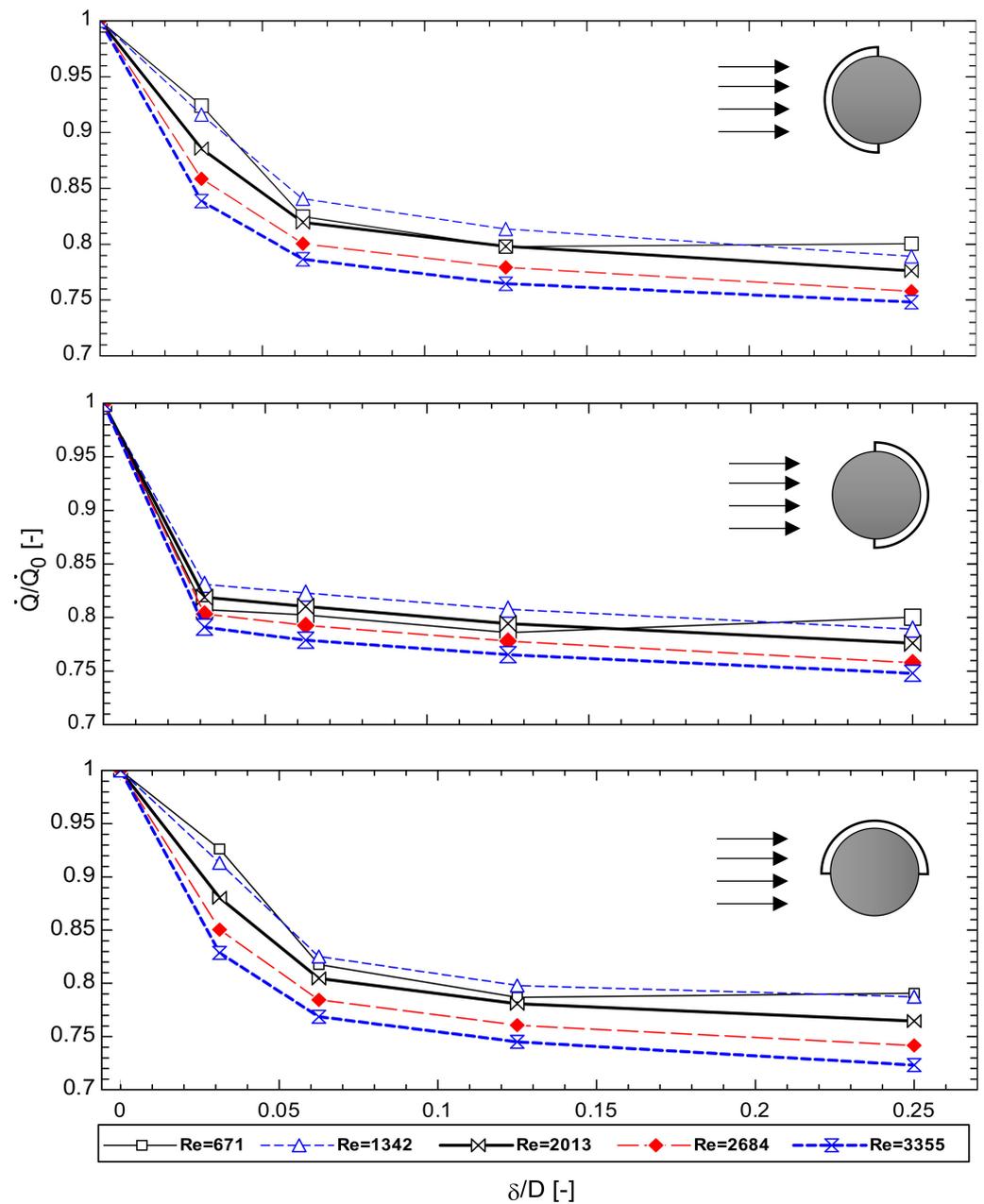
Figure 10. Heat transfer rate ratio in the function of dimensionless gap thickness.

For the rear-positioned slit at *Re* = 671 $\dot{Q}/\dot{Q}_0$ values are below these for *Re* = 2013. One can see a nearly monotonic decrease of the heat transfer rate ratio with increasing gap thickness, being the sharpest in the lower δ/D range and reaching practically a plateau for $\delta/D > 0.1$. The data points are connected by a piecewise linear function, instead of polynomial fit, because higher-order curve fitting produced slight inflection in the plateau range, which was a misleading artifact of the method.

A clearer picture of how the flow velocity influences heat transfer emerges from Figure 11. A decreasing trend of $\dot{Q}/\dot{Q}_0$ is seen with increasing Reynolds number, excluding the smallest Re departing from this pattern. In the range of *Re* > 1342, there is a nearly linear negative slope. However, in the span of *Re* = 671–1342, the decrease of heat transfer rate ratio is smaller or even there is a reverse trend (increase), indicating there can be a change of the flow regime. The curve for the smallest gap is placed remarkably higher than the other ones for the side and front location. Other δ/D cases, for all slit positions, exhibit

similar trends, with the $\delta/D = 0.125$ curve approaching or even crossing $\delta/D = 0.25$ with decreasing *Re*.
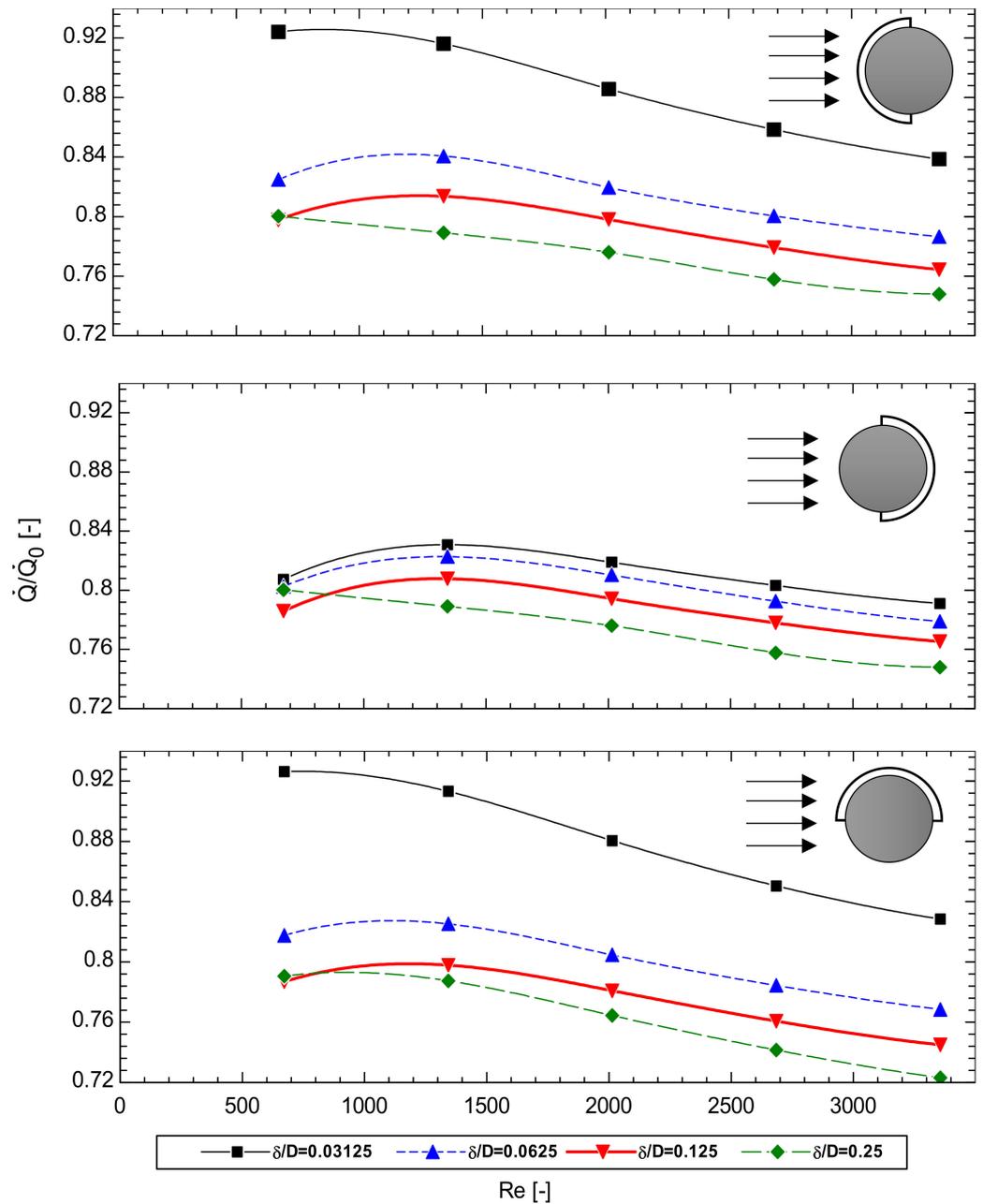
Figure 11. Heat transfer rate ratio in the function of Reynolds number.

The influence of the dimensionless gap position $\theta/180°$ on the $\dot{Q}/\dot{Q}_0$ is addressed in Figure 12. In the case of the smallest gap, the front and side locations exchange nearly equal heat transfer rates, with a significant decrease that can be seen for slit in the back ($\theta/180° = 1$). For the rest of the considered gap thicknesses, there are very small differences between the tube circumference and gap locations. The weak dependence in the range of $\delta/D = 0.0625$–0.25 is the most evident for the highest $Re = 3355$. The back and front slit cases indicate moderately higher, nearly equal thermal throughputs relatively similar to the side example.
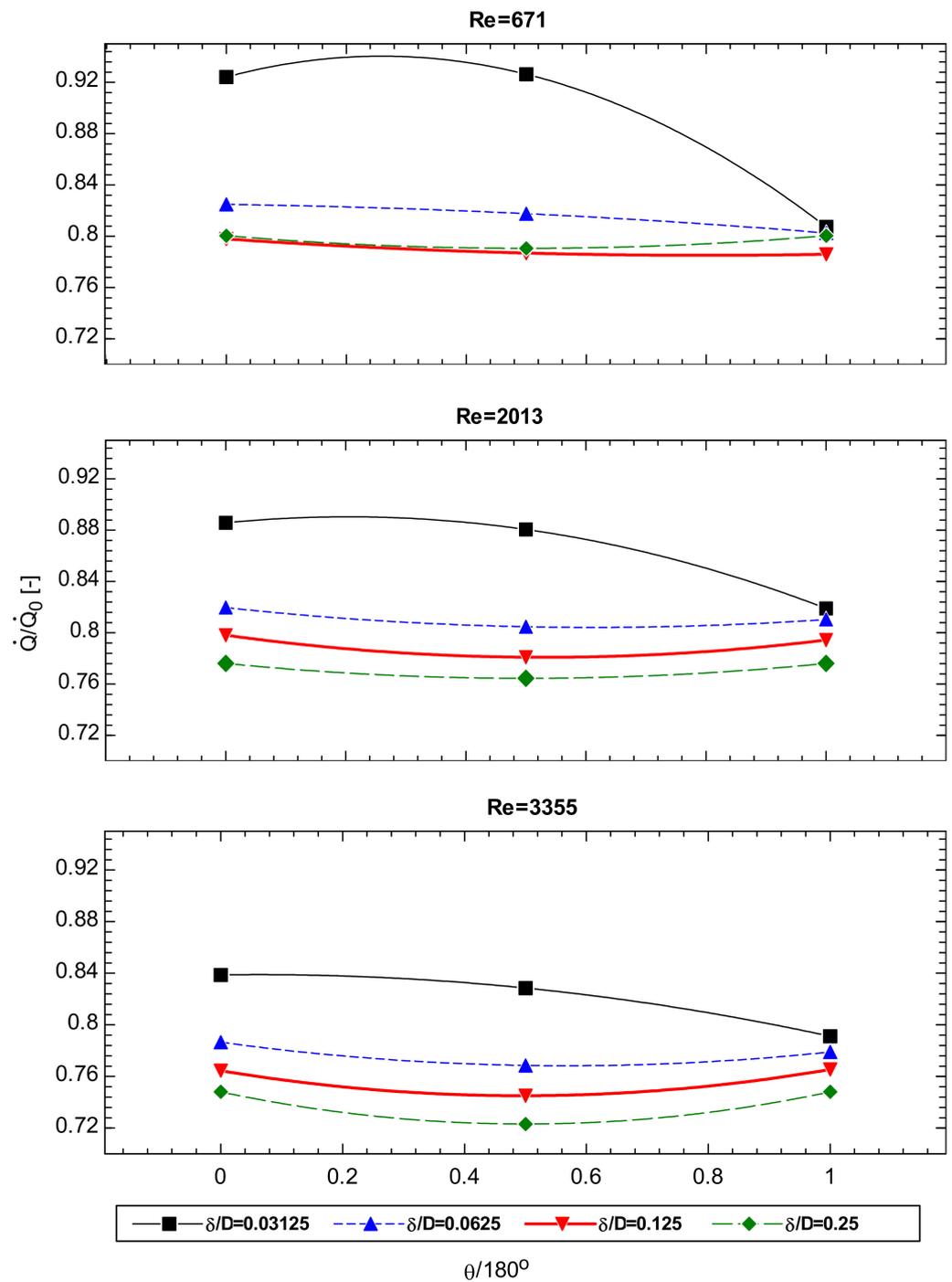
Figure 12. Heat transfer rate ratio in the function of gap position.

In Figure 13, the ratio of mean heat transfer coefficient with the gap presence to heat transfer ratio without any fin discontinuity is presented in the δ/D function. The front and side location results in enhancement of the mean convective heat transfer for the smallest discontinuity. This effect is not present in the rear location. For the remaining δ/D values, h/h_0 is below 1.0 (decrease of h). Besides, the local maximum at $\delta/D = 0.03125$ heat transfer coefficients ratio decreases nonlinearly with the increasing gap thickness, except for $\delta/D = 0.25$ where a slight increase can be observed. For the rear slit location, there is no local maximum and h/h_0 is at an approximately constant level of 0.9.
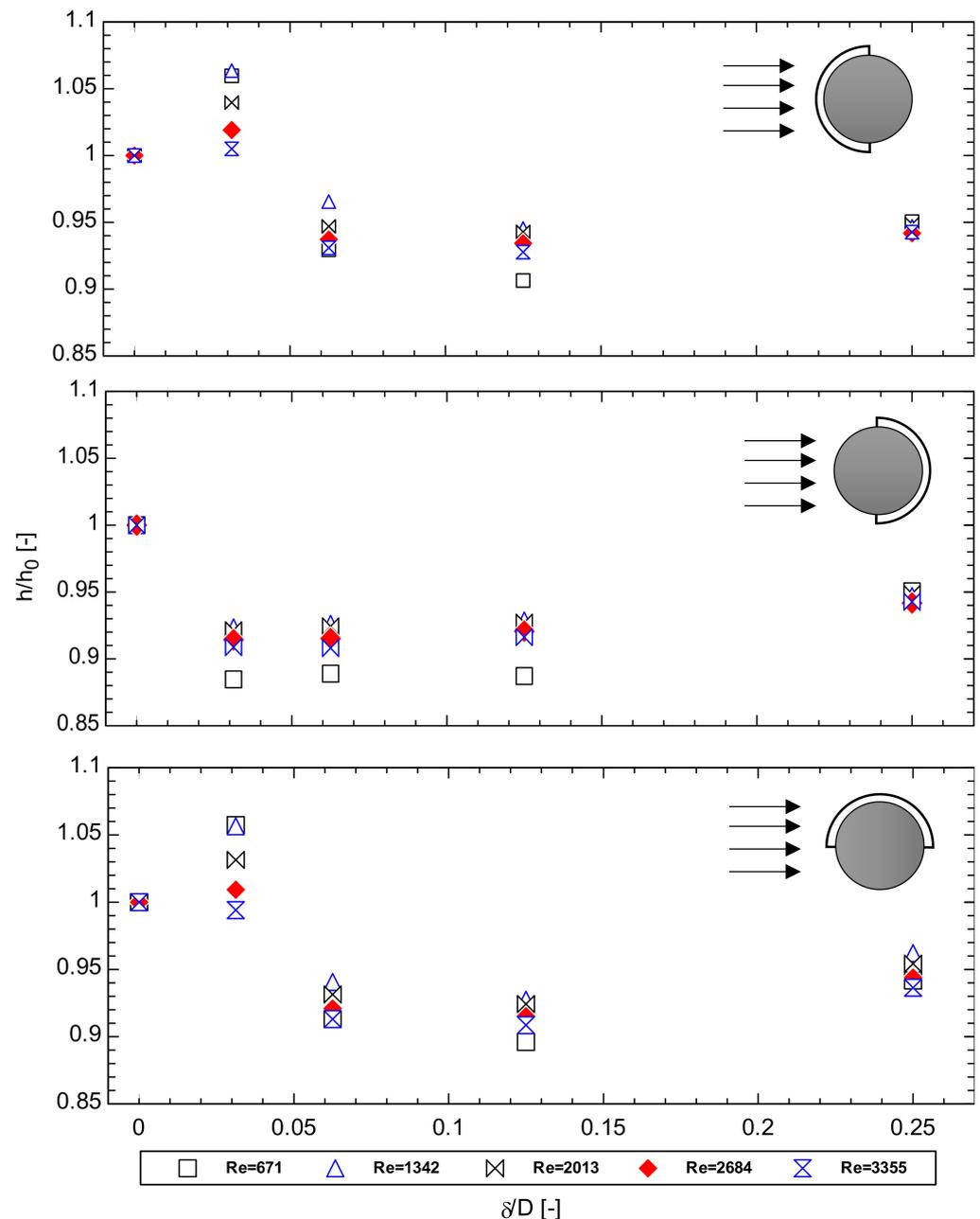
Figure 13. Heat transfer coefficient ratio in the function of dimensionless gap thickness.

In Figure 14, the h/h_0 dependence on the Reynolds number is shown. For the side and front cases at $\delta/D = 0.03125$, the convective heat transfer enhancement is existing at the whole range of Re numbers. For all slit thicknesses, there is a weak decrease of h/h_0 with the increase of the flow velocity. The smallest discontinuity heat transfer coefficients diverge from the wider gap cases, being at least 4% higher, whereas for the rest of the example values are adjacent to each other. There is not any enhancement for the rear position; the highest h/h_0 are noted for $\delta/D = 0.25$ at a nearly constant value of $h/h_0 = 0.95$ for the whole range of Reynolds numbers, diverging from the rest of the considered cases. At the lowest Re, for the remainder examples, the h/h_0 reaches a minimum of approx. 0.88, with a local maximum at $Re = 1342$, and for the rest of the volumetric flow range there is a decrease with the increase of Re.
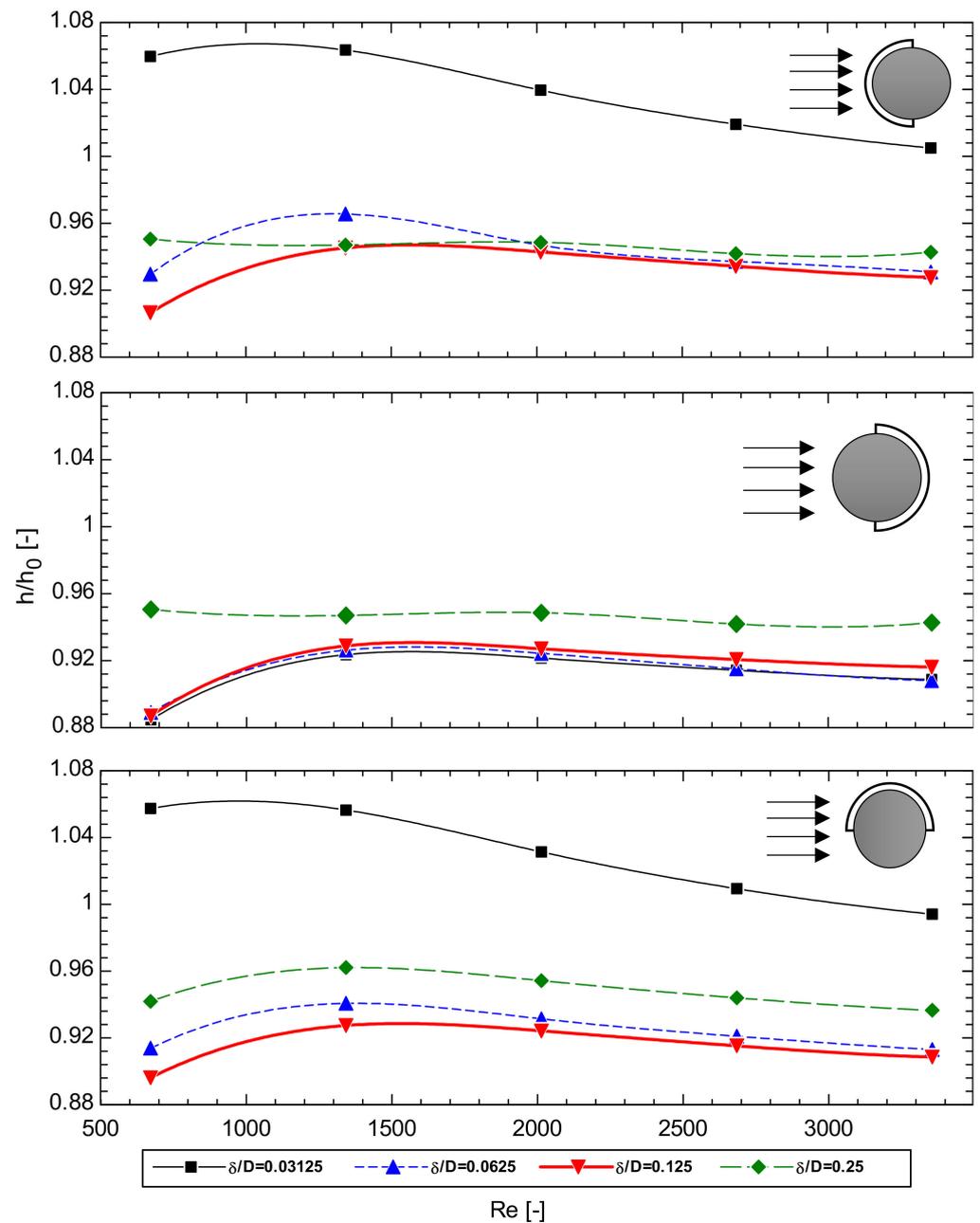
Figure 14. Heat transfer coefficient ratio in the function of Reynolds number.

The dependence on the gap position is shown in Figure 15. At $\delta/D = 0.03125$, there is the highest difference between the front, side, and back locations. The remaining slit thicknesses exhibit a very weak dependence on $\theta/180°$, typically slightly reducing, with a maximum for the front and minimum for the back case.
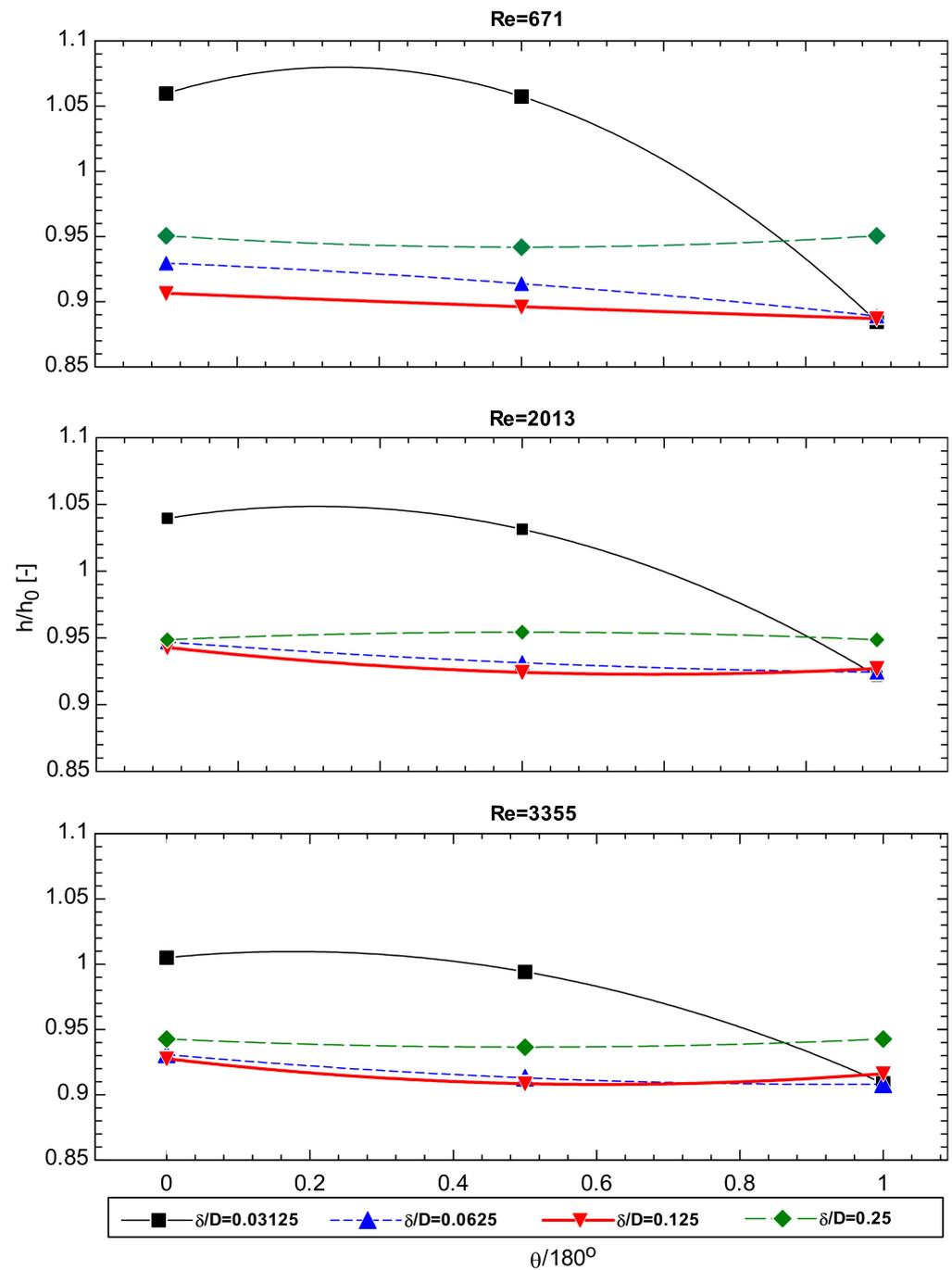
Figure 15. Heat transfer coefficient ratio in the function of the gap position.

In Figure 16, the contour map of a local heat transfer coefficient, which is defined as:

$$h_x = \frac{\dot{q}}{T_f - T_{in}},$$ (16)

where T_{in} is periodic inlet air temperature, is presented for different gap sizes at the lowest Reynolds number ($Re = 671$) for front fin discontinuity location. Figure 16 was arranged to investigate the convective heat transfer enhancement relatively to no gap case. Intensification is present for the thinnest slit ($\delta/D = 0.03125$)—for bigger gaps, this effect diminishes (Figure 10). The contours are similar for all cases shown; therefore, the analysis starts with a description of common map characteristics. There is a high h_x zone

at the inlet edge of the fin—this is the region where the thermal boundary layer is the thinnest. The area of this region is reduced at the center because of the presence of the fluid circulation flow spanning from the leading edge of the fin to the surface of the tube (Figure 17). This circulation is caused by the trace flow downstream of the upstream tube—being a result of boundary layer detachment. In Figure 17, one can see the circulation regions visualized by streamlines. The circulation area is wider in the rear region of the fin (behind the tube) than upstream of the tube (air flows from the bottom to the top in Figure 17). Because the circulating fluid moves with reduced velocity, local heat transfer coefficients are significantly lower. On the sides of the tube, air flows with increased velocity (Figure 17)—this corresponds to the high h_x region in Figure 16 (contour level: 4, h_x = 18–24 W/m^2/K).

Figure 16. h_x map on the surface of the fin for various gap sizes at Re = 671 for the front location of the gap.
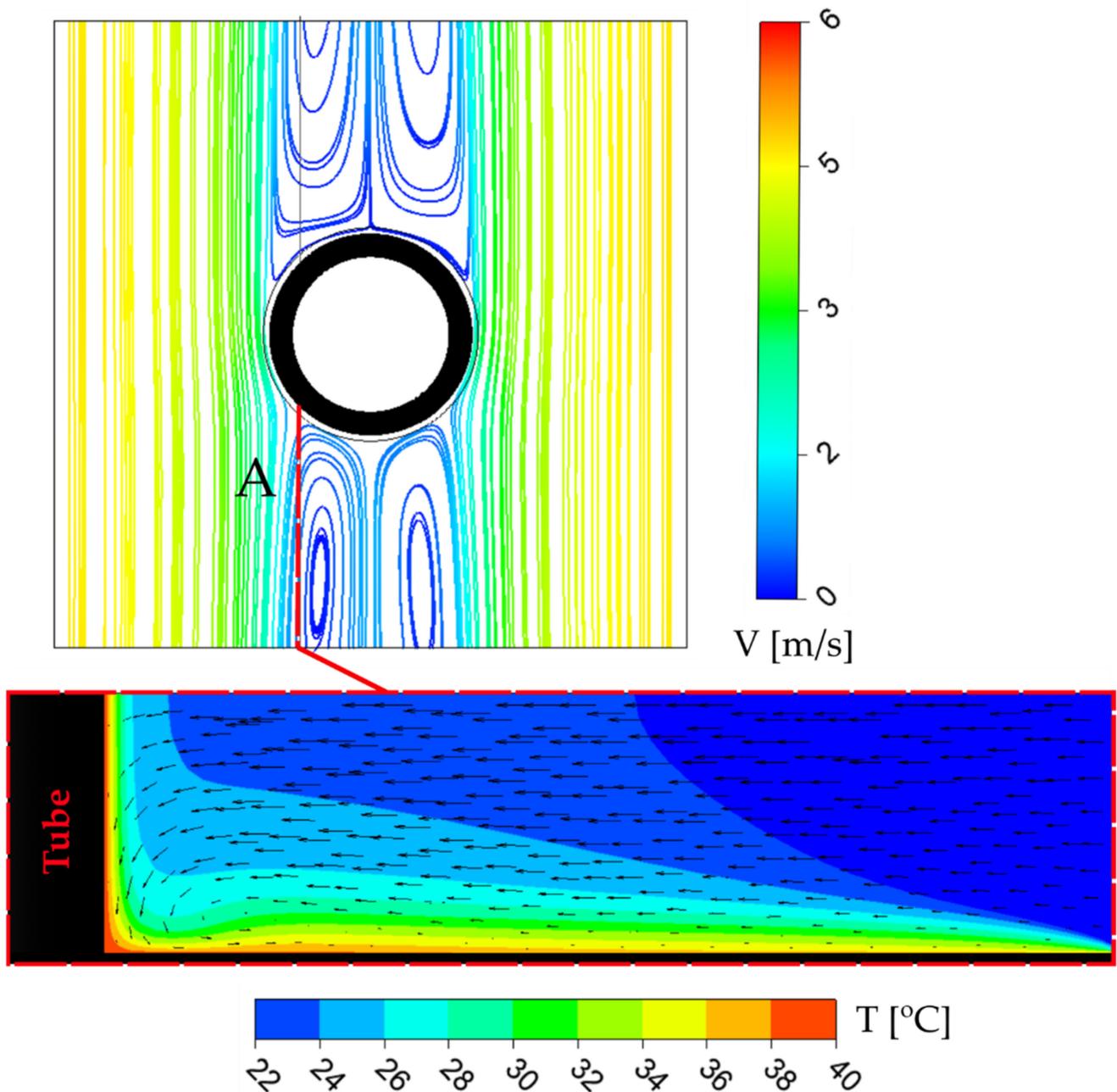
Figure 17. The top view of streamlines with the vector field showed on the face A upstream of the tube, at *Re* = 2013, for the ideal tube-fin contact case.

At the fin surface zone near the front part of the tube circumference, there are two bands of intensified heat transfer (placed symmetrically on the sides). This local enhancement is caused by a horseshoe vortex, which is visible in Figure 17, where the velocity vector field is visualized at plane A. The swirl of the fluid can be observed at the base of the tube. For the one-row or staggered arrangement plate-fin tube heat exchangers, the horseshoe vortex spans the whole half of the tube's circumference. In the present analysis, periodic flow simulations are equivalent to the inline arrangement. Therefore, the wake behind the preceding tube divides the horseshoe vortex in two (Figure 16—$\delta/D = 0$). There is also a thin region of enhanced heat transfer coefficient at the trailing edge, widening at the middle of the fin. This is the effect of the implementation of periodic heat transfer conditions in the simulations. Because the negative heat flux is set on the outlet, the small backflow of colder fluid causes this "artificial" heat transfer intensification. This effect

is practically of the same magnitude for all cases—it cancels in the comparative analysis. Even the h_x contour maps share the same characteristics; for $\delta/D = 0$, the strength of the heat transfer enhancement caused by the horseshoe vortex is the greatest. With the increase of the gap thickness, the horseshoe intensification becomes weaker. The thinnest slit covers partially the area of vortex action, whereas in the $\delta/D = 0.125$ case the vortex is present completely over the gap, which results in only moderately increased local h on the edges of the fin discontinuity. The introduction of the gap improves the heat transfer on the leading edge of the fin and changes somewhat the flow and heat transfer characteristics in the region downstream of the tube.

For $\delta/D = 0.03125$ and $\delta/D = 0.0625$, this alteration is not significant, yet for $\delta/D = 0.125$ there is a dramatic change—low heat transfer coefficient region (contour 3 in Figure 16) doubles its size and merges with the smaller one at the upstream part of the tube. The combined effect of the enhancement on the leading edge with still strong horseshoe vortex intensification can explain the observed augmentation of mean HTC for the thinnest slit relatively to no-gap example (Figure 13). The mean of heat transfer enhancement with thin slits cut in the front of the tube (for low airflow velocities) should be further studied. It could be a promising method of heat transfer intensification in compact heat exchangers.

The enhancement of h_x, by the presence of the slit, relative to ideal fin-tube contact example is not enough to cancel the negative effects of the fin discontinuity at its base (tube-fin junction)—in Figure 11 one can observe at least 6% lower heat transfer rate in the respect to $\delta/D = 0$. In Figure 18, the most obvious consequence of the introduction of the gap can be seen—the blockage of heat flow in the fin area adjacent to the discontinuity. This effect is visualized by dimensionless temperature excess Θ contour map, where:

$$\Theta = \frac{T_f - T_{in}}{T_w - T_{in}}. \tag{17}$$

The fin is the most isothermal for the no-gap example, and the contour map is the most symmetrical. In Figure 18, the heat flux blockage is evident for the cases with the gap—Θ is significantly lower for nearly half of the fin on the side of the slit. For the gap in the front, the reduction of temperature is the smallest, while for the side location it is the highest (lowest fin efficiency). The mean h on the sides of the fin is the highest, and that is the reason for the severe temperature decrease. The Θ is the biggest on the average for the front case because the heat flux is directed backward (low h_x region) and the enhancing effect of the horseshoe vortex in the front of the tube is partially blocked. Analyzing the back gap position, the Θ is significantly lower on average. Heat flux is directed towards the front where the heat transfer intensification regions cause effective cooling of the fin. The result is substantially lower fin temperature in the back. In a conclusion, the gap placement in the front blocks the heat flow in the direction of the enhanced convective heat transfer area, which is not beneficial, although it results in higher fin efficiency than for the gap in the back. This can explain why there is a sudden heat transfer rate ratio drop for the rear slit position. The effect of low fin efficiency seems to combine with poorer convective heat transfer relatively similar to other discontinuity placement cases (Figure 10). The side gap position is the worst of the considered positions in terms of the fin temperature contour. The colder fin area is slightly bigger than the gap in the back. As the heat flux is directed to the side where high-velocity flow increases the intensity of heat transfer, the fin is efficiently cooled there. As the mean heat transfer coefficient is nearly as high as for the gap in the front, $\dot{Q}/\dot{Q}_0$ is slightly lower than the front gap for thin slits. The enhanced convective heat transfer compensates for the low fin efficiency. Figure 19 shows the influence of the flow Reynolds number on the h_x. The h_x contour maps are presented at four Reynolds numbers for a 1 mm thick gap in the back. The heat transfer intensification caused by the presence of the horseshoe vortex is less significant for the lowest Re, and it gets increasingly distinctive as the airflow velocity increases. The thermal boundary layer becomes thinner at the leading edge of the fin with the raising Re, which is visible as the wider high h_x area. As the Re increases, the h_x contours change their values proportionally, but the overall

topology (shape of the contours) is analogous for all airflow velocities. In Figure 14, one can see that for $Re = 671$ h/h_0 is the lowest—this is mainly caused by the low activity of the horseshoe vortex (Figure 19).

Front gap position

Side gap position

Back gap position

Ideal tube-fin contact

$\Theta:$ 0.75 0.77 0.79 0.81 0.82 0.84 0.86 0.88 0.90

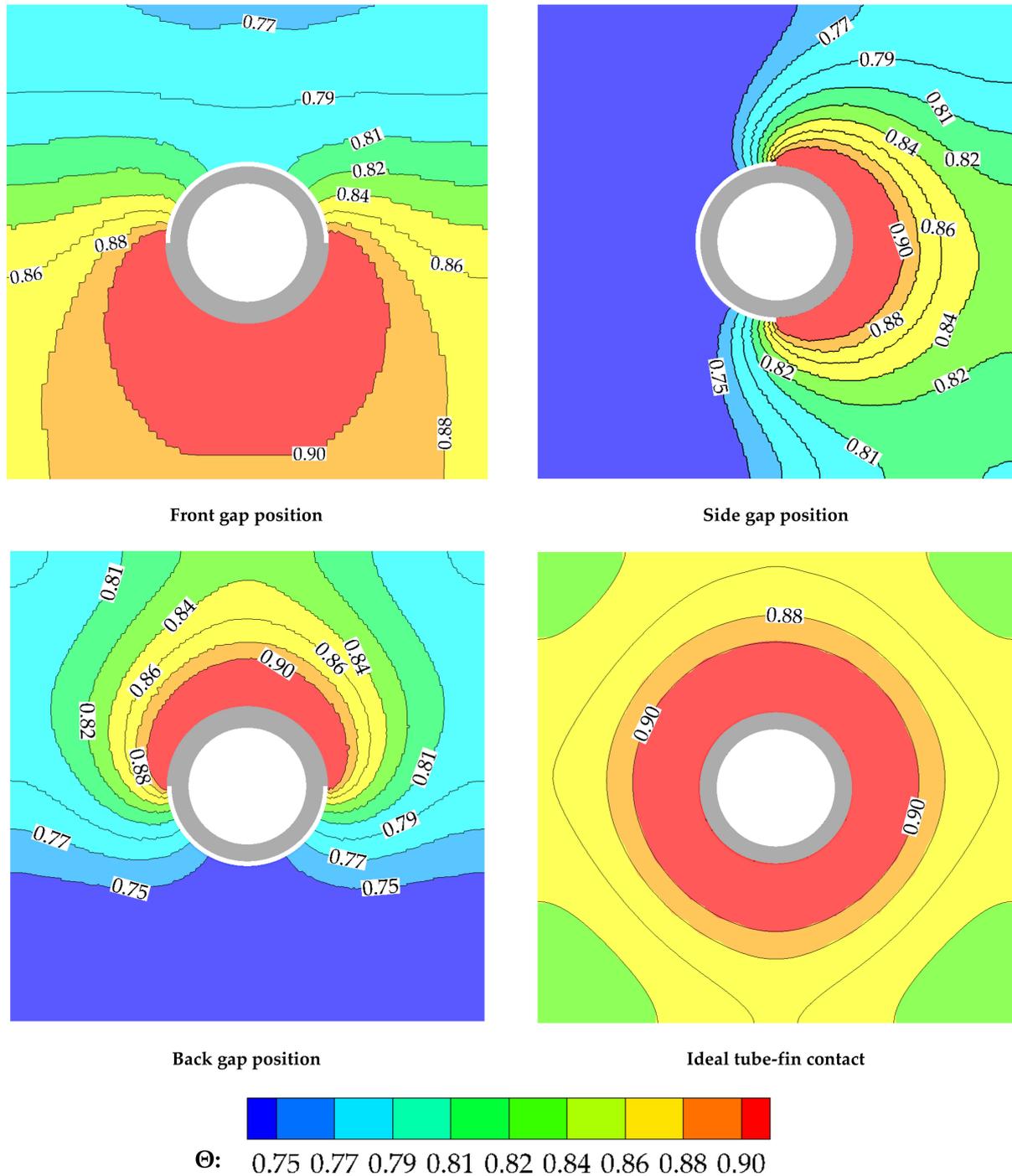**Figure 18.** Dimensionless temperature excess Θ contour at $Re = 2013$ and $\delta/D = 0.03125$ for different gap positions.

Re=671

Re=1342

Re=2013

Re=2684

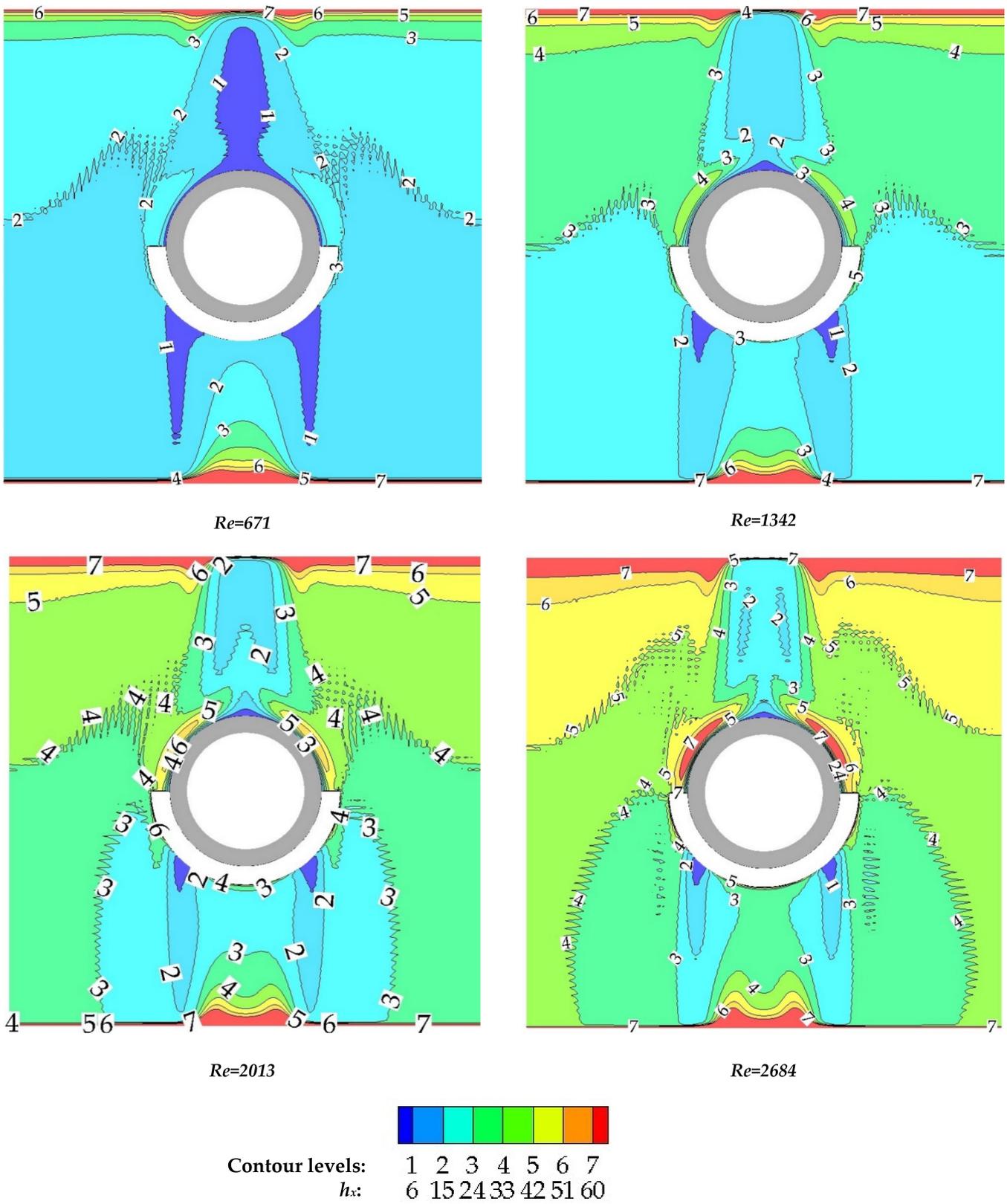Contour levels:　1　2　3　4　5　6　7
h_x:　6　15　24　33　42　51　60

Figure 19. h_x map on the surface of the fin for various Reynolds numbers, with the gap size: δ/D = 0.125 and back gap position.

4. Conclusions

To sum up the key findings from the numerical simulation, the fin discontinuity along the circumference reduces the heat transfer rate relatively to the perfect fin-tube contact case. The placement of the gap reduces the skin friction locally to zero, which can promote beneficial flow structures, which causes enhancement concerning the no-gap case, especially for small slit sizes. However, the convective heat transfer enhancement is overpowered by the heat flux blockage effect which leads to $\dot{Q}/\dot{Q}_0 < 1$ for all the cases. Fin discontinuity in front of the tube causes the smallest reduction of the heat transfer rate in comparison to the ideal tube-fin contact, especially for thin slits. Even the heat transfer rate ratio minimum is obtained for the gap at the side position (approx. 0.72), it performs slightly worse for the small gap range than the front location. The rear gap is characterized by the mean $\dot{Q}/\dot{Q}_0 = 0.8$ for all the gap sizes and therefore is considered the worst scenario, without the advantage of the smallest gap range. For gaps wider than $\delta/D > 0.1$, the heat transfer rate reduction becomes nearly constant for a specified Reynolds number. Generally, the higher the airflow, the $\dot{Q}/\dot{Q}_0$ becomes lower. For multirow plate-fin tube heat exchangers with small fin discontinuities, reversing the flow direction can result in an even 15% heat transfer increase if most of the gaps are in the rear of the tube (low airflow velocity). Realistically, obtaining this maximum is not very probable, although the present study shows that reversing the flow can have a positive effect on the plate-fin tube heat exchanger performance, and its longevity depends on the nature of the origin of the discontinuities (are they, and how fast they enlarge). The convective heat transfer enhancement for thin slits in the front should be further investigated to test the possibility of the introduction of fin cut-outs as heat transfer intensification structures in compact heat exchangers.

Author Contributions: Conceptualization, A.N.G. and M.Ł.; methodology, A.N.G. and M.Ł.; software, G.G.; validation, M.Ł., A.N.G. and D.A.; writing—original draft preparation, M.Ł. and D.A.; writing—review and editing, G.G.; visualization, D.A.; supervision, A.N.G. All authors have read and agreed to the published version of the manuscript.

Data Availability Statement: Not applicable.

Conflicts of Interest: The authors declare no conflict of interest.

Nomenclature

A	finned side heat transfer surface, m^2
A_{t0}	bare outside tube surface, m^2
CFD	computational fluid dynamics
c_p	specific heat at constant pressure, J/kg/K
d	diameter, m
d_h	$(4\cdot(L_f - D)\cdot L_t\cdot L_f)/(2\,[L_f^2 - (\pi\cdot D^2/4)] + \pi\cdot D\cdot L_t)$—hydraulic diameter, m
D	outer diameter of the tube
e	total fluid energy, J/kg
g	gravitational acceleration, m/s^2
h	heat transfer coefficient, W/m^2/K
h_x	local heat transfer coefficient
$h_\%$	$(h_i - h_{i-1})/h_i$, relative change of heat transfer coefficient, %
k	$0.5\cdot u_i{'}\cdot u_i{'}$—kinetic energy of turbulence m^2/s^2
L	length, m
$\overline{L}$	periodic length vector, m
$\dot{m}$	mass flow, kg/s
n	heat-mass transfer analogy exponent
$\overline{n}$	vector normal to a surface
Nu	Nusselt number

p	pressure, Pa
$\tilde{p}$	periodic pressure, Pa
Pr	Prandtl number
Pr_t	turbulent Prandtl number
$\dot{q}$	heat flux (vector), W/m^2
$\dot{Q}$	heat transfer rate, W
$\bar{r}$	position vector, m
Re	$V \cdot d_h / v$—Reynolds number
Ri	$(g \cdot \beta \cdot \Delta T \cdot L)/V^2$—Richardson number
Sc	Schmidt number
Sh	Sherwood number
SST	shear stress transport
T	temperature, K
$\tilde{T}$	periodic temperature, K
V	average velocity (scalar), m/s
u	velocity vector, m/s
$\bar{u}$	time-averaged velocity vector, m/s
x	cartesian coordinates vector, m
X_t	tube spacing, m
Y^+	non-dimensional distance between the first mesh node and the wall

Greek symbols

β	volumetric expansion coefficient, 1/K
δ	gape thickness, thickness, spacing, m
δ_{ij}	Kronecker delta
Δ	difference of a quantity
θ	the gap placement angle
Θ	temperature excess
λ	thermal conductivity, W/m/K
μ	dynamic viscosity, kg·m/s
v	kinematic viscosity, m^2/s
ρ	density, kg/m^3
$\rho\overline{u_i u_j}$	Reynolds stresses, Pa
σ	linear temperature gradient, K/m
τ_{ij}	stress tensor, Pa/m
ω	specific dissipation rate, 1/s

Subscripts

0	zero gap thickness
ave	average
d	based on the tube outside diameter
f	fin
g	gap
i	inside, inner, for i-th mesh refinement
i, j, k	indices (1, 2, 3)
in	inlet
o	outlet, outer
t	tube, turbulent
w	wall

References

1. Gorecki, G. Investigation of two-phase thermosyphon performance filled with modern HFC refrigerants. *Heat Mass Transf.* **2018**, *54*, 2131–2143. [CrossRef]
2. Chai, L.; Tassou, S. A Review of Airside Heat Transfer Augmentation with Vortex Generators on Heat Transfer Surface. *Energies* **2018**, *11*, 2737. [CrossRef]
3. Taler, D.; Taler, J.; Trojan, M. Experimental Verification of an Analytical Mathematical Model of a Round or Oval Tube Two-Row Car Radiator. *Energies* **2020**, *13*, 3399. [CrossRef]
4. Lotfi, B.; Sundén, B.; Wang, Q. An investigation of the thermo-hydraulic performance of the smooth wavy fin-and-elliptical tube heat exchangers utilizing new type vortex generators. *Appl. Energy* **2016**, *162*, 1282–1302. [CrossRef]

5. Välikangas, T.; Karvinen, R. Conjugated Heat Transfer Simulation of a Fin-and-Tube Heat Exchanger. *Heat Transf. Eng.* **2018**, *39*, 1192–1200. [CrossRef]
6. Bansal, P.; Wich, T.; Browne, M. Optimisation of egg-crate type evaporators in domestic refrigerators. *Appl. Therm. Eng.* **2001**, *21*, 751–770. [CrossRef]
7. Blygold Blygold—Example of Galvanic Corrosion Damage. Available online: https://www.blygold.com/services/coil-coating/ (accessed on 15 May 2021).
8. Critoph, R.; Holland, M.; Turner, L. Contact resistance in air-cooled plate fin-tube air-conditioning condensers. *Int. J. Refrig.* **1996**, *19*, 400–406. [CrossRef]
9. Jannick, P.; Meurer, C.; Swidersky, H. Potential of Brazed Finned Tube Heat Exchangers in Comparison to Mechanical Produced Finned Tube Heat Exchangers. In Proceedings of the International Refrigeration and Air Conditioning Conference, West Lafayette, IN, USA, 16–19 July 2002.
10. Zhao, H.; Salazar, A.J.; Sekulic, D.P. Analysis of Fin-Tube Joints in a Compact Heat Exchanger. *Heat Transf. Eng.* **2009**, *30*, 931–940. [CrossRef]
11. Jeong, J.; Nyung Kim, C.; Youn, B.; Saeng Kim, Y. A study on the correlation between the thermal contact conductance and effective factors in fin–tube heat exchangers with 9.52 mm tube. *Int. J. Heat Fluid Flow* **2004**, *25*, 1006–1014. [CrossRef]
12. Cheng, W.; Madhusudana, C. Effect of electroplating on the thermal conductance of fin–tube interface. *Appl. Therm. Eng.* **2006**, *26*, 2119–2131. [CrossRef]
13. Taler, D.; Ocłoń, P. Thermal contact resistance in plate fin-and-tube heat exchangers, determined by experimental data and CFD simulations. *Int. J. Therm. Sci.* **2014**, *84*, 309–322. [CrossRef]
14. Taler, D.; Cebula, A. A new method for determination of thermal contact resistance of a fin-to-tube attachment in plate fin-and-tube heat exchangers. *Chem. Process Eng.* **2010**, *31*, 839–855.
15. Singh, S.; Sørensen, K.; Condra, T.J. Influence of the degree of thermal contact in fin and tube heat exchanger: A numerical analysis. *Appl. Therm. Eng.* **2016**, *107*, 612–624. [CrossRef]
16. Saboya, F.E.M.; Sparrow, E.M. Local and Average Transfer Coefficients for One-Row Plate Fin and Tube Heat Exchanger Configurations. *J. Heat Transf.* **1974**, *96*, 265. [CrossRef]
17. Menter, R.F. Zonal Two Equation Kappa-Omega Turbulence Models for Aerodynamic Flows. In Proceedings of the 23rd Fluid Dynamics, Plasmadynamics, and Lasers Conference, Orlando, FL, USA, 6–9 July 1993.
18. Lindqvist, K.; Skaugen, G.; Meyer, O.H.H. Plate fin-and-tube heat exchanger computational fluid dynamics model. *Appl. Therm. Eng.* **2021**, *189*, 116669. [CrossRef]
19. Taler, D.; Ocłoń, P. Determination of heat transfer formulas for gas flow in fin-and-tube heat exchanger with oval tubes using CFD simulations. *Chem. Eng. Process. Process Intensif.* **2014**, *83*, 1–11. [CrossRef]
20. Jasiński, P.B. Numerical study of the thermo-hydraulic characteristics in a circular tube with ball turbulators. Part 2: Heat transfer. *Int. J. Heat Mass Transf.* **2014**, *74*, 473–483. [CrossRef]
21. Ocłoń, P.; Łopata, S. Study of the Effect of Fin-and-Tube Heat Exchanger Fouling on its Structural Performance. *Heat Transf. Eng.* **2018**, *39*, 1139–1155. [CrossRef]
22. Ansys Inc. *ANSYS CFX Theory Guide*; Ansys Inc.: Canonsburg, PA, USA, 2013.
23. Shevchuk, I.V.; Jenkins, S.C.; Weigand, B.; Von Wolfersdorf, J.; Neumann, S.O.; Schnieder, M. Validation and analysis of numerical results for a varying aspect ratio two-pass internal cooling channel. *J. Heat Transf.* **2011**, *133*. [CrossRef]
24. Siddique, W.; El-Gabry, L.; Shevchuk, I.V.; Fransson, T.H. Validation and Analysis of Numerical Results for a Two-Pass Trapezoidal Channel With Different Cooling Configurations of Trailing Edge. *J. Turbomach.* **2012**, *135*. [CrossRef]
25. Goldstein, R.J.; Cho, H.H. A review of mass (heat) transfer measurements using naphthalene sublimation. *Exp. Heat Transf. Fluid Mech. Thermodyn.* **1993**, *10*, 21–40. [CrossRef]
26. Kays, W.M.; William, M.; London, A.L.; Alexander, L. *Compact Heat Exchangers*; Krieger Pub. Co.: Malabar, FL, USA, 1998; ISBN 1575240602.
27. Rosman, E.C.; Carajilescov, P.; Saboya, F.E.M. Performance of One- and Two-Row Tube and Plate Fin Heat Exchangers. *J. Heat Transf.* **1984**, *106*, 627. [CrossRef]
28. Tecplot Inc. *Tecplot.360 EX User's Manual*; Tecplot Inc.: Bellevue, WA, USA, 2018.
29. Saboya, S.M.; Saboya, F.E.M. Transfer coefficients for plate fin and elliptical tube heat exchangers. In Proceedings of the 6th Brazilian Congress of Mechanical Engineering, Rio de Janeiro, Brazil, 15–18 December 1981.
30. Stephan, P. B1 Fundamentals of Heat Transfer. In *VDI Heat Atlas*; Springer: Berlin/Heidelberg, Germany, 2010; pp. 15–30.